POLITECNICO
MILANO 1863

SCUOLA DI INGEGNERIA INDUSTRIALE
E DELL'INFORMAZIONE

Aerodynamic analysis of cyclists: a novel approach combining CFD and rigging animation technique

Tesi di Laurea Magistrale in
Aeronautical Engineering - Ingegneria Aeronautica

Giacomo Antenucci, 970933

Advisor:
Prof. Paolo Schito

Co-advisors:
Marco Rossoni
Claudio Somaschini

Academic year:
2022-2023

Abstract: Reduction of aerodynamic drag is a crucial aspect in cycling. Currently, to optimize aerodynamic, athletes rely on wind tunnel tests, CFD simulations, or velodrome experiments, which still require validation through wind tunnel measurements. This implies that each new test necessitates significant investments in terms of financial resources and time, a vital aspect in a cyclist's professional life. This paper introduces a novel workflow that aims to streamline and accelerate the aerodynamic analysis process for cycling. The proposed workflow focuses on utilizing a full-sized mannequin and integrates CFD simulations, solved with 3D RANS and k-ω SST model, wind tunnel validation, 3D scanning, and rigging animation techniques in Blender. The animation technique involves creating a virtual skeleton that allows the scanned model to be posed in any desired position, eliminating the need for physical adjustments and repetitive wind tunnel testing. To showcase the time-saving advantages of this approach, a steady CFD analysis is conducted to compare six different configurations obtained using the rigged model, in terms of drag areas, velocity streamlines, and pressure coefficient distribution. The obtained data trends closely align with previous similar studies in the literature. The entire process, from the initial 3D scanning of the mannequin to achieving the desired positioning, takes approximately three hours, significantly reducing the time required compared to traditional methods. Additionally, future adjustments to the position or equipment can be easily made using the virtual rigging model. By integrating virtual techniques with CFD simulations and wind tunnel validation, the proposed workflow enables rapid evaluation of aerodynamic performance in a more efficient and cost-effective manner.

Key-words: Cycling aerodynamics, 3D scan, CFD, Rigging, Wind tunnel, Cyclist position

1. Introduction

Nowadays, aerodynamics is one of the key factors in improving cycling race performance. Especially at the professional level, the main quest is the reduction of aerodynamic drag, that at racing speed contributes up to 90% of the total resistance force that athletes must contend with [12, 24]. Until now, the aerodynamics of a cyclist can be investigated using three approaches: wind tunnel testing, velodrome testing and Computational Fluid Dynamics (CFD).

Wind Tunnel

Since the late 1800s, wind tunnels have served as the primary proving ground for testing and improving the aerodynamics of various objects. In recent times, their significance has expanded to include cycling, where they are widely utilized as a validation tool for CFD results [4, 10, 11, 17], as well as a standalone tool [14]. Wind tunnels offer several advantages, such as the ability to measure drag, side forces, ambient air pressure, real-time air temperature, and wind speed. The flow in a wind tunnel is controlled, both in terms of direction and wind speed, independently of the natural weather conditions outside the tunnel. This ensures consistent and reliable results that can be theoretically repeated and verified, something that is challenging to achieve in outdoor testing. However, the main drawback is that there are no standardized testing protocols for wind tunnels and without universal protocols there's no way of guaranteeing consistent and comparable results between one wind tunnel test and another [20].

Velodrome

Also Velodrome tests have been proven reliable in detecting changes in the aerodynamic drag in cyclists [23] and for physic test for the athlete [10]. However the ambient conditions are unpredictable: density, temperature and pressure are parameters that cannot be controlled and are subject to the current weather. In addition, it is difficult to have a constant flow in direction and intensity. Besides this obstacles, important contributes have been brought by Notio Aerolab [27], that with on-bike aerometer provides accurate data on the drag area. This allows the athlete to adjust position and equipment, and see the effect on the aerodynamic performance.

CFD

The use of Computational Fluid Dynamics is widely spread across the cycling industry as it offers the possibility to recreate desired test conditions in a virtual setting. This allows tests to be conducted without requiring the physical presence of the athlete. A wide range of simulations can be performed, with a primary focus on the aerodynamics. The cyclists's performance can be measured in relation to the peloton [7], the influence of vehicles [5], cross-wind conditions [21], as well as different positions and equipment [6]. In this researches, all cyclists have static legs and no pedaling effect is taken into account. Although not very realistic, the aerodynamic drag of a pedaling cyclist, averaged over one pedaling revolution, is quite similar to that of the same cyclist with the crank almost horizontal [15]. Regarding turbulence modelling, RANS combined with the SST k-ω model shows the best overall performance for these type of analysis [18]. Although LES outperforms all other RANS turbulence models and provides in addition information on the unsteady flow field [21], it however imposes a much higher computational cost (about 5-15 times more than RANS, depending on the RANS turbulence model used), which makes the RANS SST k-ω model more attractive from a practical point of view [6, 8, 29]. Nevertheless, CFD remains only an incomplete tool as wind tunnels continue to be the gold standard for aerodynamic testing in the foreseeable future. However, this procedure is often time-consuming and can pose difficulties in terms of accessibility for the cyclist. Elite athletes have busy schedules during the season, and finding the time, even for a couple of days required for the tests, and potentially traveling to the wind tunnel location can be complex. Additionally, test days can be physically tiring. Furthermore, conducting tests in wind tunnels represents a significant financial investment as well.

In recent times, the use of 3D scanners has gained traction in addressing some of these issues. 3D scanning digitally recreates physical components in a simulated world with exact dimensions, gathering raw data as point cloud information and converting it into user-friendly formats like CAD model. The applications of this technology are constantly increasing in the industrial manufacturing due to its portability, readiness-to-use and accuracy [25]. Body scanning has also started to gain popularity, despite the limitations involved in producing accurate geometries for input into numerical simulation [13], particularly in the sports industry. In the cycling field, elite teams have already started to rely on scanning technology. The Italian National cycling team designed a tailor-made handlebar [30], which Pinarello manufactured as a unique piece tailor-made to each athlete's arms to achieve a perfect rider-bicycle relationship. Scanning proved to be fundamental in providing precise measurement of the anatomic part of interest of the body, necessary for virtual creation of the handlebar. Moreover, in many studies [8, 9, 29], scanning provides the virtual model of the athlete used for CFD simulations. The cyclist is scanned in their racing position, on the bike, static. Within a few minutes the scanning process is completed, generating a virtual model (in the form of a point-cloud) in the scanning software. The model is then post-processed and exported for CFD simulations, eliminating the need for the athlete's physical presence during the aerodynamic simulations, as now they are computed virtually, significantly reducing their commitment. In addition to that, the virtual model is printed and tested in wind tunnels for measurement validation. 3D printing is one of the main of focus of elite teams: Vorteq [33] exploit this technology to develop the world's fastest skin-suit. The scanner aims to digitally capture the rider's exact anatomy, which takes only a

few minutes. After a couple of hours of post-processing the scan, the computational draping system, in collaboration with with Vorteq's skinsuit team, assembles the skinsuit. Additionally, the scan is utilized for 3D printing anatomically-precise mannequins of athletes, eliminating the need for them to return for additional tests when creating new skinsuits. Further analysis utilizes 3D mannequin of athletes as substitutes for conducting wind tunnel aerodynamic tests directly with real cyclist. The main advantages stems from the fact that when a live rider is present in the wind tunnel, there is a "wiggle" factor to contend with, as the rider may move slightly, and that's going to affect the results. Only a perfect still mannequin allows for precise measurements. However, a mannequin is inherently motionless, thereby eliminating the pedalling effect. Professional cyclists have already embraced this approach. Team Giant-Alpecin and the TU Delft scanned Tom Dumoulin's body using 150 DSLR cameras, capturing numerous pictures of the body from many different angles, simultaneously, taking around 30 minutes. Subsequently, a 3D mannequin of his body was printed [19]. The drag of this mannequin, each time with a different suit, was then tested and optimized in the TU Delft's wind tunnel. In the same context team Jumbo-Visma chose to develop a mannequin of Primoz Roglic [32] for testing clothing. The main effort lies in the post-processing of the amount of data: alignment, smooth and simplification of the scans, and mesh closure. With a 3D printed mannequin ideally there is unlimited access to the athlete, allowing for comprehensive wind tunnel testing and the development of a perfect suit tailored specifically to them. These research efforts highlight the significant advantage that scanning technology brings, as having a virtual and precise model of the cyclist enables conducting a wide range of tests without the need for direct involvement of the athlete, thus saving time and resources. Moreover, scanning plays a crucial role in performing CFD simulations, as a virtual model of the athlete, obtained through 3D scanning, is required for the computations. The printed model can then be used for wind tunnel validation.
This paper aims to develop a new workflow for studying cyclist aerodynamics, integrating the scan technology, CFD and wind tunnel testing. The process begins with a full-size mannequin in a perfectly still and standing position. The model is then 3D scanned and converted into a virtual representation. After undergoing post-processing, a significant advancement beyond previous work is achieved by animating the character using the rigging animation technique on Blender. Widely used in animation, this technique allows the virtual model to be positioned in any desired posture, as long as an appropriate skeleton is generated [1, 3]. Once the mannequin is transformed from its original position to a cyclist position, the virtual model is integrated with a bike, and the mesh is prepared for CFD testing. Furthermore, the virtual model is 3D printed and appropriately scaled to validate measurements in the wind tunnel.

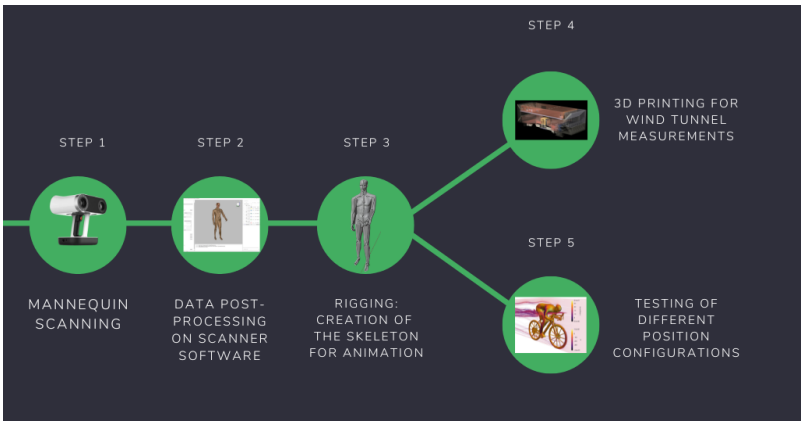

Figure 1: Workflow of the research process.

The paper is structured as follows: Section 2 describes the workflow for creating the printed model. Section 3 presents the wind tunnel setup for conducting the test on the singular configuration. In Section 4, CFD simulations are performed to ensure for grid independence and evaluate five cyclist configuration. The results are compared to the original configuration. Finally, Section 5 provides a summary, conclusions, and outlines future works.

2. Model realization

2.1. 3D scanning

The starting point of the work consisted of the scanning of a life-sized mannequin. The model was available in the Virtual Prototyping Laboratory at Politecnico di Milano, with a height about 1.80 m, and it was positioned

in a standing position with the arms slightly forward-facing. The mannequin was completely naked, without any hair. Artec Leo 3D [2] scanner was selected to perform the operations. It is an arm-based, cable-free scanner, with a capture rate of 80 fps and 3D resolution up to 0.2 mm. The data were directly transferred into the Artec Studio 15 software, where the various frames were post-processed. The characteristics of the scanner made the scanning process easier, as there was no need to carry around a laptop or power supply. Initially, a test scan was conducted on a singular arm. The test scan was necessary to familiarize with the instrument and software, as well as to identify potential sources of errors. The texture option was disabled for all scans, since it was not of major interest in this work and would have increased the amount of data generated. The main problem consisted in the correct positioning of the target, since the scanner light must diffused uniformly across the arm's surface. Once this operation was achieved, the whole mannequin was ready to be scanned. It should be noted that the position of the mannequin was not ideal for scanning, since there were certain areas shaded. This led to difficulties in capturing the whole surface of the body, as observed in the case of the arm.

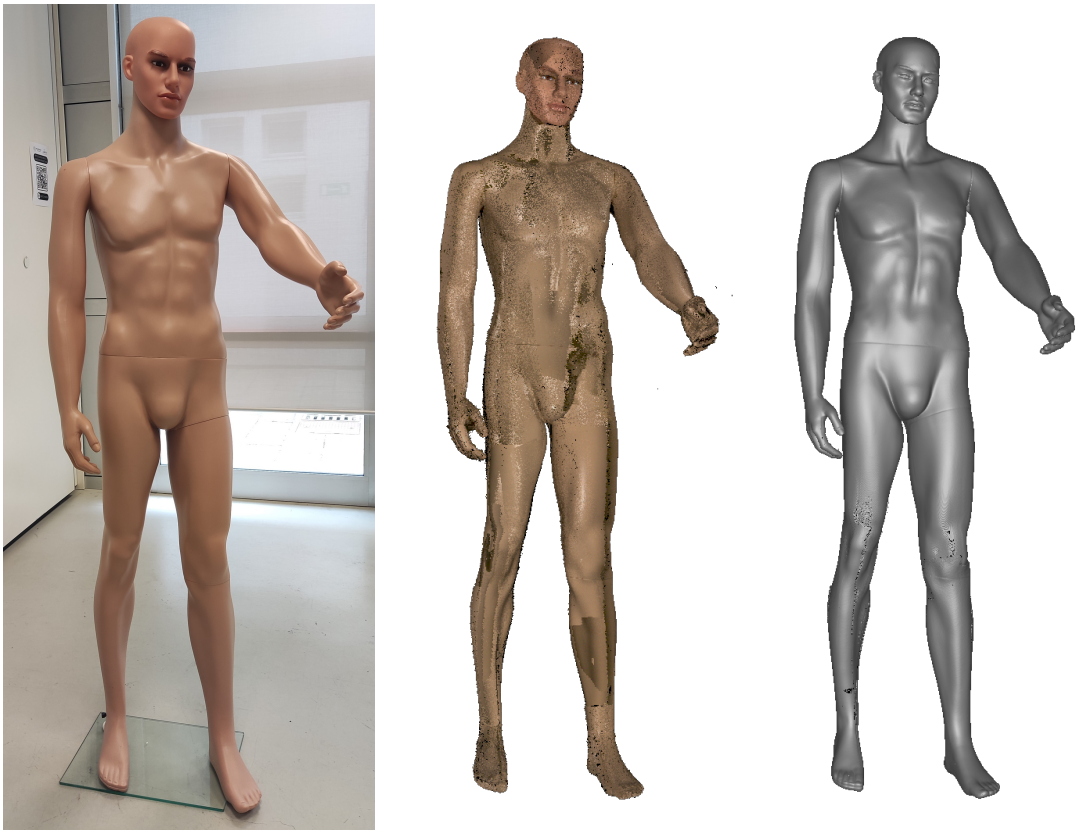

(a) (b) (c)

Figure 2: Evolution of mannequin representation: (a) physical mannequin used as a reference, (b) scanned frames and (c) final 3D model generated by the smooth fusion.

Initially, a single scan was performed; the Artec Leo 3D was pointed at the body from an appropriate distance (ranging from 0.35 m to 1.2 m) and moving it up and down while sliding it sideways. The goal was to avoid capturing the same area more than twice. Conducting only one scan would have saved time and, consequently, resulted in less amount of data generated and to be post-processed. In addition, the phase of scan alignment performed on Artec Studio would have been avoided. However, it was not possible to cover the entire body surface with just one scan. The frame generated lacked in accuracy and resulted in a mesh with several holes. To address this issue, multiple scans were performed by taking advantage of the fact that the mannequin was composed by five removable parts: the head, two arms, torso and legs. Beside the scan of the torso, the head and the arms were removed from the mannequin and scanned individually. Another final scan was necessary to capture the bottom part of the feet. The amount of data generated was obviously more consistent than the previous case, but nearly the whole surface of the mannequin was covered. The advantage of conducting multiple scans became evident. From the moment the mannequin was placed until the last scan, fifteen minutes had elapsed. With more practice, this time could be reduced. In the case with a live rider, it would be possible to position the model in a better way, with the arms and legs spread apart to minimize the shaded areas to cover.

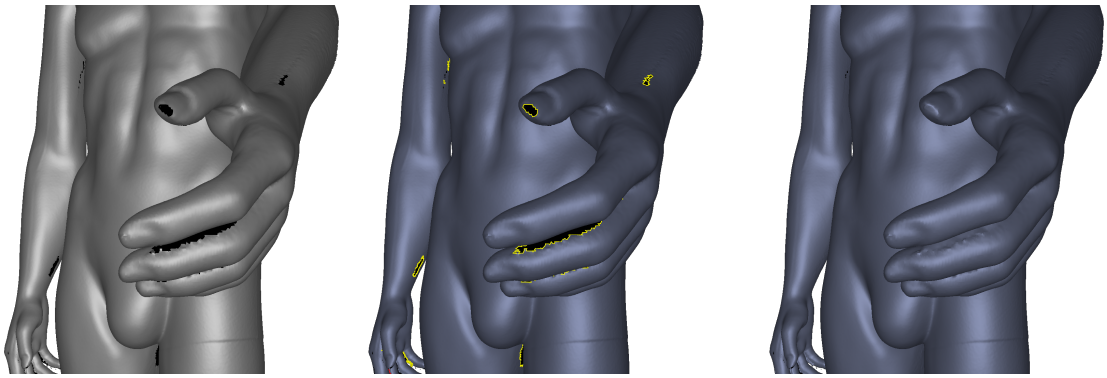

(a) (b) (c)

Figure 3: Zoomed-in view of the hole filling process in Artec Studio 15, focusing on the hands zone: (a) Mesh with holes, (b) Selected holes, (c) Holes filled.

The point cloud generated by the 3D scanner was then post-processed with Artec Studio 15. Specifically five point clouds were imported, one for each scan. Naturally, there were multiple frames representing the same area from different scans. Deletion of duplicated frames significantly dragged down the data-weight, along with deletion of the frames which did not reach the minimum accuracy requested by the scanner software of 1 mm. The next stage consisted in the aligning of the different scans. This was easily accomplished using the automatic tool in Artec Studio. By indicating the positions of the same three points in the different scans, the software aligned the frames. Therefore, fine and global registration were carried out, which respectively automatically and precisely aligned captured frames, and converted all one-frame surfaces to a single coordinate system using information on the mutual position of each surface pair. These were mandatory tasks to ensure the accuracy of the resulting mesh. The smooth fusion algorithm was used to process the first mesh. This algorithm creates a polygonal 3D model, by melting and solidifying the captured and processed frames. However, the initial mesh generated at this stage had a closure problem, meaning it was not fully closed. To resolve this issue, a dedicated tool was employed for hole filling, as depicted in Fig. 3. Therefore, the mesh simplification algorithm was applied to significantly decrease the amount of memory occupied by the model. This involved removing triangles with edge lengths less than 0.05 mm.

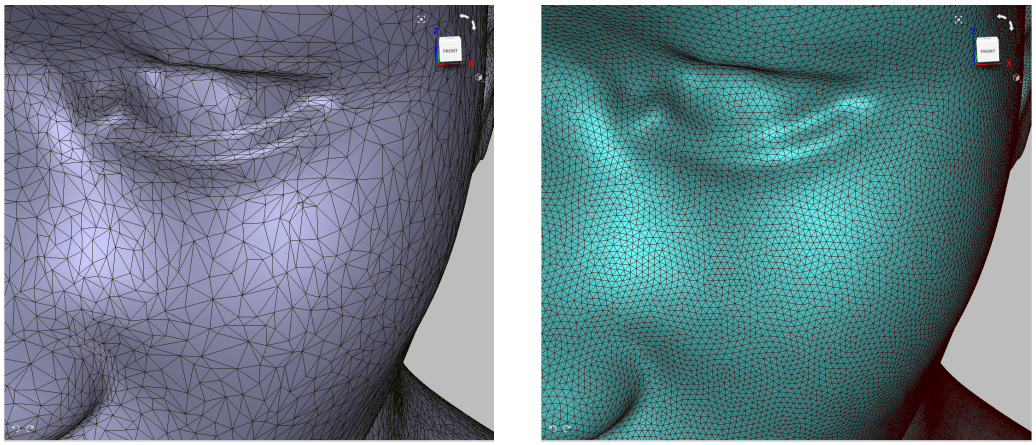

(a) (b)

Figure 4: Isotropic remeshing process in the facial area: (a) mesh before isotropic remeshing, (b) result after applying isotropic remeshing with uniform-sized triangles.

Finally, the model underwent remeshing using the isotropic remesh tool to ensure the new triangles had uniform sizes, as shown in Fig. 4. This resulted in an output file smaller than the original one due to the presence of uniform triangles. After completing these tasks, the resulting mesh was ready for the rigging process. No additional scans were needed since the inherently motionless nature of the mannequin eliminated the potential errors caused by even minor changes in positions, which are common with live riders. The post-processing operations, which culminated in the export of the 3D model, took approximately two hours. The duration of this process was heavily influenced by the computational power of the computer used to execute the algorithms..

2.2. Rigging

The bridge between the scanned mannequin, which was standing, and placing the model on a bike in the cyclist position was achieved through the rigging technique. This technique is used in skeletal animation, which is a part of to the digital animation. The 3D character is represented in two parts: a surface representation of the model, which is the mesh, and a hierarchical set of interconnected digital bones (the so called skeleton or rig) used to animate the mesh. The rigging process involves creating the bone structure for the model, which is used for manipolation and free movement [16]. Each bone is created independently and can be transformed in position, rotation, and scale. However, to establish a skeletal structure, there must be a hierarchical relationship among the bones, where each bone is connected to its parent or child bones. The bone structure is simple: it consists of a rigid shape with two spherical hinges at each end (tail and head). Two bones are typically connected in two ways: either the tail hinge of one bone coincide with the head hinge of the other bone or the distance between two hinges is kept constant. The interaction between the bones and the mesh is governed by a weight scale. Each bone has a certain influence over a section of the mesh, so that when the bone is moved or rotated, the corresponding part of the mesh deforms to follow the transformation. The body should move in a realistic way; hence weight painting is a fundamental part of the rigging process. Weight painting involves digitally painting the areas of the mesh where the influence of the bone should be accurately represented. The software automatically generates the weights, but some of the time corrections are needed. Once the model is rigged, there are two approaches to move it: forward and inverse kinematics. In robotics this normally refers to calculate the relations between end-effectors and joint angles. So, for forward kinematics, the joint angles are the inputs, the outputs would be the coordinates of the end-effectors.

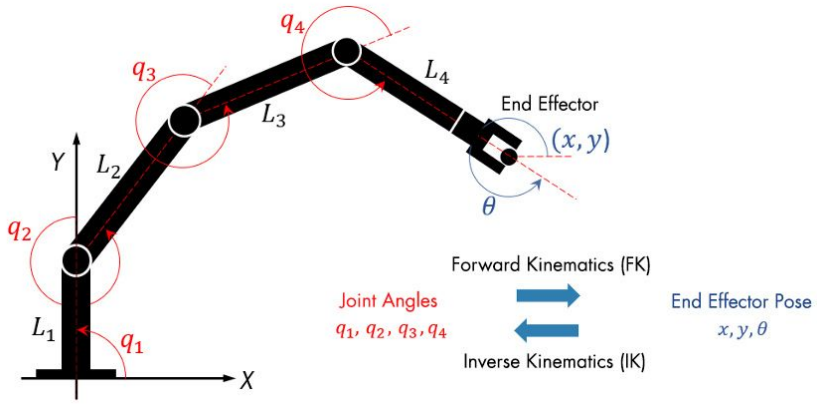

Figure 5: Configuration of joint positions of a robot using forward and inverse kinematics.

For inverse kinematics, the given inputs are the coordinates of the end-effectors, the outputs to calculate are the joint angles. Forward kinematic implies that rotating a bone will cause all its child to follow the rotation. With inverse kinematic it is lost the ability to animate every bone of the chain separately, but it is gained the ability to animate the whole chain with the end-effector only. For the rigging process, the software used was Blender, a free open-source software known for its versatility and user-friendliness.
The first step was the creation of the rig for the scanned isolated arm; the rig was generated with fifteen bones, and similarly to the workflow used in the scanning process this test helped to become familiar with the software. Once the rig was set the arm was moved to verify whether the automatically generated weight system required any corrections. Weights are visualized using a gradient with cold and hot colors, such that areas of low value (weights close to 0.0) are displayed as blue (cold) and areas of high value (weights close to 1.0) are displayed as red (hot). All in-between values are displayed as rainbow colors (blue, green, yellow, orange, red). Fig. 6 shows the movement system of the isolated arm implemented to bend the lower arm. As the arm moves, the mesh area around the highlighted bone is deformed, accordingly to the weight system.

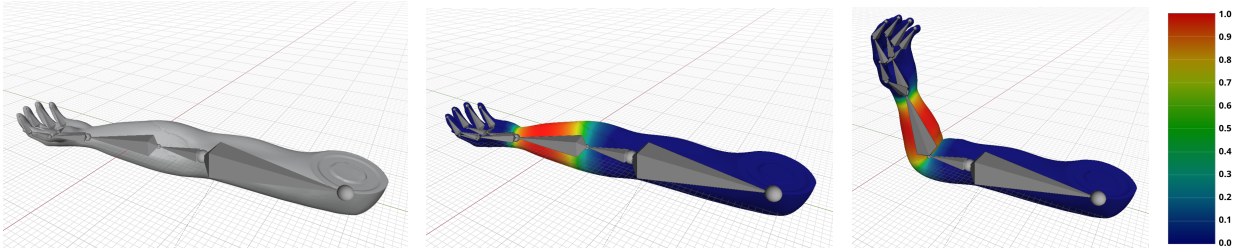

Figure 6: Example of motion and weight painting system for isolated arm with colorbar in Blender.

After this test, the 3D model of the mannequin was imported to begin the actual work. Two options were available for rigging it, and both were pursued to determine the better approach. The first option involved creating a custom rig specifically for the model, while the other option utilized the default rig automatically generated by the software. The first procedure was straight-forward, as it allowed for easy creation and placement of bones along the mannequin. Moreover, there was total freedom in generating the inverse kinematic connections. However, these connections were complex to make, especially for a human body. Therefore, the default rig provided by the software was used. It was first re-scaled in order to fit the dimension of the mannequin. The number of bone was 25, distributed across the whole body, plus 40 additional bones for representing hand movements. Although this number was an approximation compared to the actual 206 bones in the human body, it still offered a good compromise for replicating the main movements of the mannequin.

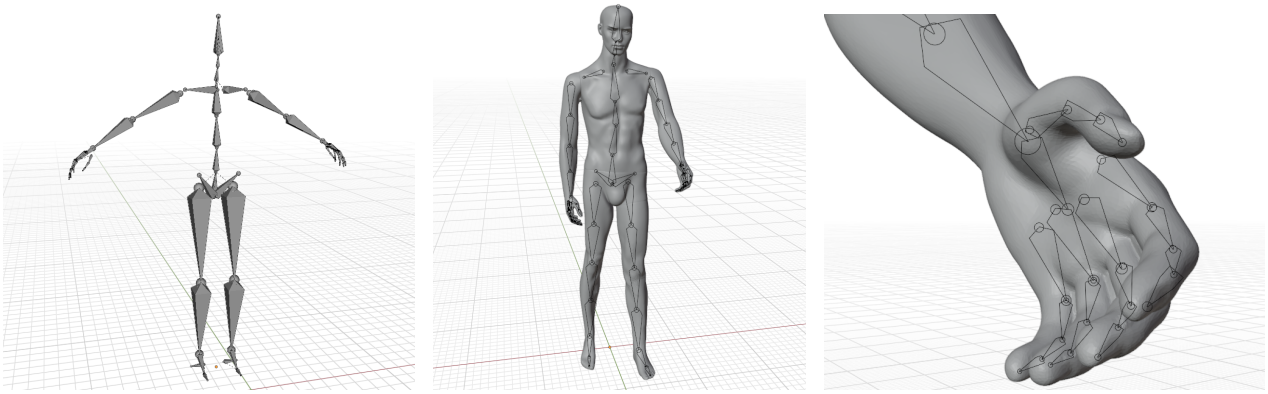

Figure 7: Default rig in Blender and rig modified and adjusted to fit the specific proportions of the mannequin. A zoomed-in view of hand rig is also represented.

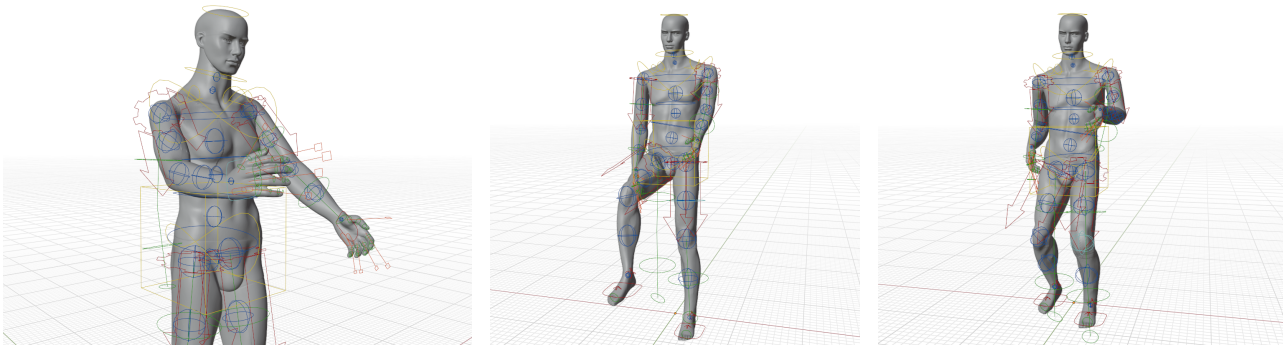

(a) (b) (c)

Figure 8: Movement of three end effectors captured in three images: (a) is the movement of the right hand, (b) the movement of the right leg, and (c) the movement of the torso.

Each bone was then placed in its corresponding location along the mannequin. This was the most challenging step to face: the initials rig were correct at first glance, but when the model was moved there were inadequacies in the deformed mesh. One of the main reason was the initial asymmetric position of the model. This made it

difficult to accurately position the bone hinges, and even a millimetric change in their placement resulted in a significant difference in the motion of the mannequin. Once the various hinges were correctly aligned to mimic the real human joints, the rig was generated. This also automatically created the inverse kinematic connections, with the five major connections being for the hands, feet and torso. These were the connections that allowed to drive the model in whatever position it was required: just grabbing one of those end-effector all of the chain (e.g. for the hand the whole arm) moved accordingly.
In Fig. 8 it is shown the motion of three end-effectors: the right hand and leg and the torso, which are freely positioned. The rest of body follows a movement of one end-effector. Alongside the generation of the rig, the weights for each bone were set automatically, although some modifications were needed. With the weight painting tool it was possible to get the accurate amount of influence for each bone to their mesh area. Areas painted to a color equal to 1 implies that the mesh follows completely the bone movement, while for areas with 0 weight the mesh remains completely still. The weight painting operation was done with the mannequin in its original position, and the main effort was to smooth the transition areas between the various weights. An additional weight modification was requested with the model placed in the final cyclist position. This was necessary to adapt the weights so that the mesh deformed in the most natural way. To create the complete model, a bicycle was required. The mannequin was integrated with an STL file of a Canyon Inflite racing bike, which was resized to match the dimensions of the mannequin. Utilizing the automatically generated inverse kinematic links, the model was manipulated to achieve desired movements using the five available end-effectors. Additionally, forward kinematics was employed to rotate the fingers, feet, and a portion of the back. Through these controls, the mannequin was successfully positioned on the saddle, with hands on the handlebar and feet on the pedals. The complete process of developing and fitting the rig for the mannequin, including bone placement, hinge alignment, weight painting system correction, and cyclist animation, required a total of one hour.

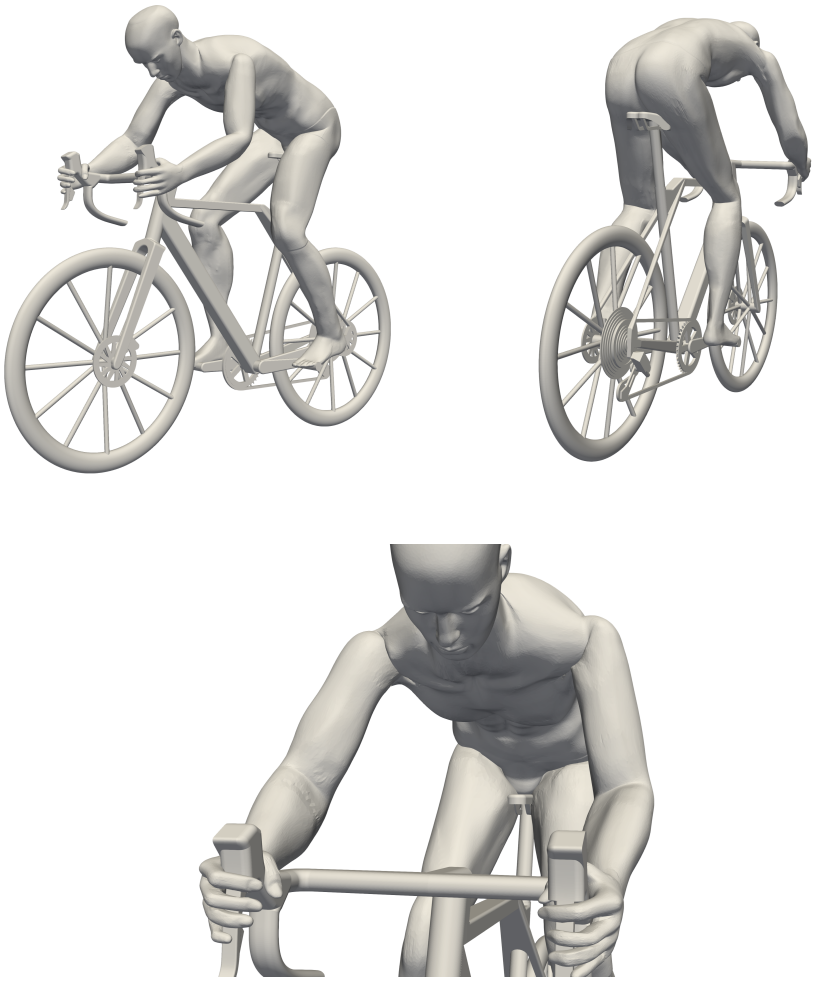

Figure 9: Perspective frontal and back views of the final position of cyclist in Blender, with zoomed-in view of the front side.

2.3. Printing

The printing operation was conducted in the Prototyping Laboratory in Politecnico di Milano (Lecco campus), with the Formiga P-110 3D Printer. The material was Nylon 12 (or PA12), a polyamide with a density of 1.01 g/cm^3. The model was scaled down to 1:4 of its actual dimensions. For a volume of 1.326×10^3 cm^3, the total weight of the model resulted in 1.397 kg.
Before any further operations, the virtual model was modified: a perforated cube was added in the correspondence of the bottom bracket. That was necessary to test the model in the wind tunnel since a rectangular spine, attached to the wind tunnel support was conceived to be plugged into the cube. This allow to align the model with the wind tunnel test section.

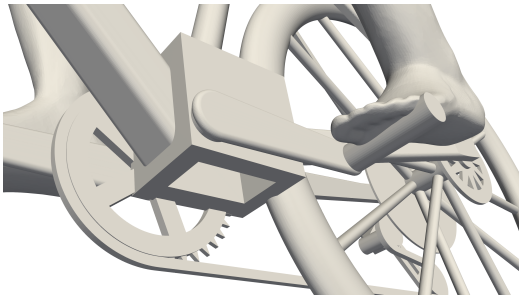

Figure 10: Zoomed view of the perforated cube on the cyclist model.

The virtual model was exported from Blender to Autodesk Netfabb, the software in which the model was prepared for the printing. In many works found in the literature, certain details of the bike were omitted, such as the crank, pedals, sprocket and chain. This was done to facilitate the printing of the model and simplify the mesh for CFD analysis. However, in this case, the printing process allowed for a high level of detail, with features as small as 0.5 mm. Since the smallest feature was the teeth of the gear wheel, bigger than the threshold, no simplification was necessary. Two steps were taken, to facilitate the printing process. Firstly, due to the large dimensions of the cyclist, the model was split into three parts. This ensured that only one batch of print was required, minimizing costs. Secondly, small tapered pins were created to serve as interconnections between the model's parts. Additionally, a layer of bi-component resin was applied to the areas where the connections needed to be made.

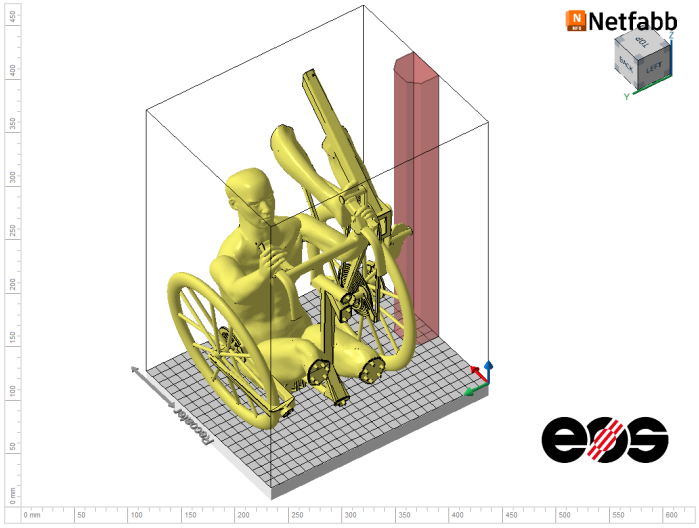

Figure 11: Printer setup of the three separated parts of the cyclist in the printer batch, as displayed in Autodesk Netfabb software.

3. Wind tunnel experiments

The wind tunnel measurements were conducted on the 3D printed mannequin of the cyclist. These measurements were essential to validate the results of the Computational Fluid Dynamics (CFD) simulations for the same model, and ensure consistency on the subsequent runs. The experiment took place in the Aerodynamic

Laboratory of Politecnico di Milano, which houses a closed circuit wind tunnel. The test section had a cross section of W×H=1.5×1 m^2 a maximum air velocity speed of 55 m/s. Since the mannequin was manufactured at a 1/4 scale, no corrections were required for the blockage ratio, which is the ratio of the projected area of the model to the test section area of the wind tunnel. The blockage ratio value of 7% was below the allowed maximum of 10% [26]. Consequently, the validation for CFD focused on comparing the drag areas, and the wind tunnel measurements only involved static forces. The primary forces of interest were the drag and the lateral force. Measurements of the vertical force was not deemed necessary, as this study primarly focused on assessing drag and lift was not a major interest.
Two S2M50 N transducers were used to measure the two forces. A proper setup was designed to attach the printed cyclist to the wind tunnel test section and the transducers. Using SolidWorks, suitable supports were created, including three aluminium supports that ensured proper alignment of the transducers with their respective measurement axes. An aluminium cylinder with a rectangular spine at the top facilitated the connection between the setup and the cyclist. The connection was achieved using a perforated cube specifically designed for this purpose. The setup was positioned such that only the cylinder protruded into the test section, while the remaining parts were positioned below the ground. This setup ensured that the aerodynamic drag was then bounded to be due to the cylinder only, which was predominantly due to the cylinder, which was designed with the smallest possible diameter to minimize interference with the measurements.
A preliminary study was conducted to estimate the magnitudes of of the forces involved. Since there is a 1:16 ratio between the forces acting on the full-size model (used in CFD) and those acting on the quarter-scale model, the preliminary analysis, including the grid independence study, provided indications of the corresponding force values, which were in the order of 1 N. These measurements also helped assess the accuracy errors associated with the transducers.

	$\mathbf{M}_b$ [Nm]	$\mathbf{F}_{lateral}$ [N]	$\mathbf{err}_{M_b}$ [%]	$\mathbf{err}_{Fl}$ [%]
Drag transducer	2.57	17.5	1.03	0.07
Lateral force transducer	4.47	39	1.79	0.16

Table 1: Estimate of bending moment and lateral force values and relative accuracy errors for the transducers.

The accuracy errors of the transducers are primarily influenced by two factors: the bending moment and the lateral force acting on them. These forces are not only generated by the aerodynamic forces on the cyclist but also by the weight of the various supports comprising the wind tunnel setup shown in the Figure below. By considering the weight and having an approximate estimation of the aerodynamic forces, it was possible to calculate the accuracy error according to the transducers' manual. Table 1 presents the value of the bending moment and lateral force acting on the two transducers, along with the corresponding error based on the transducers' specifications.

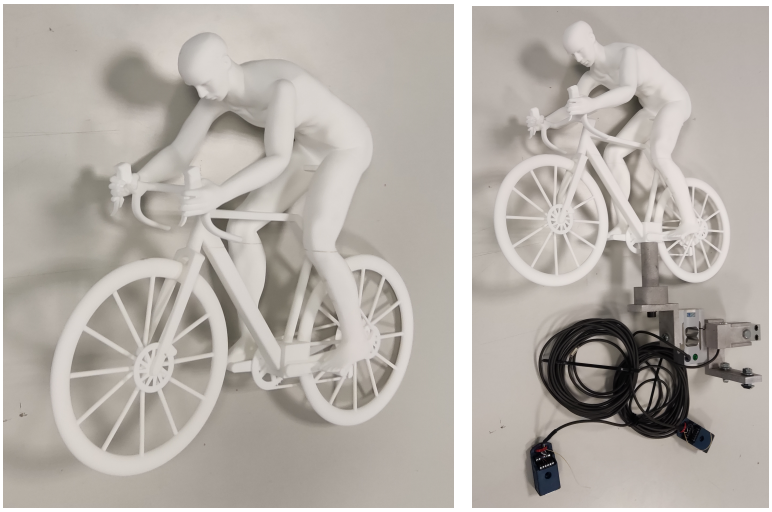

Figure 12: 3D printed model of the cyclist and model integrated with the wind tunnel setup and transducers.

Wind tunnel measurements are not reported in this paper as the tests were scheduled to be conducted after the thesis submission deadline. However, the results will be presented in the near future.

4. CFD

CFD simulations were performed for the grid independence study and for six different positions of the cyclist. All the simulations were performed in the cluster of Politecnico di Milano. CFDHub is a HPC system located in Milan, Bovisa campus, which is at disposal for intensive computations. It is shared by various research groups of the Politecnico di Milano from various departments such as Aerospace, Bio, Chemical, Energy, Environmental and Mechanical Engineering. The HPC system is Z3, which includes 143 nodes that integrates different types of multi-core Dell Intel Xeon CPUs, 2 NVIDIA K40 and 2 NVIDIA K80 GPUs, interconnected all together by Mellanox InfiniBand HDR, HDR-100 and FDR. CFDHub is a Linux based cluster.

4.1. Model

4.1.1 Computational geometry and domain

The software utilized for computational fluid dynamics was OpenFOAM. In this environment, the mesh generator employed is BlockMesh, which constructs the mesh using block-based elements. The domain size was determined based on guidelines [22], as depicted in Fig. 13, with the maximum height of the model $H_{max} = 1.44$ m. This resulted in a volume of $30.52 \times 15 \times 8.64$ m^3. The maximum blockage ratio was kept at 0.3%, which is well below the recommended threshold [26]. Due to this low blockage ratio, no corrections were made for blockage in the CFD simulations. All simulations were conducted with the cyclist in a static position.

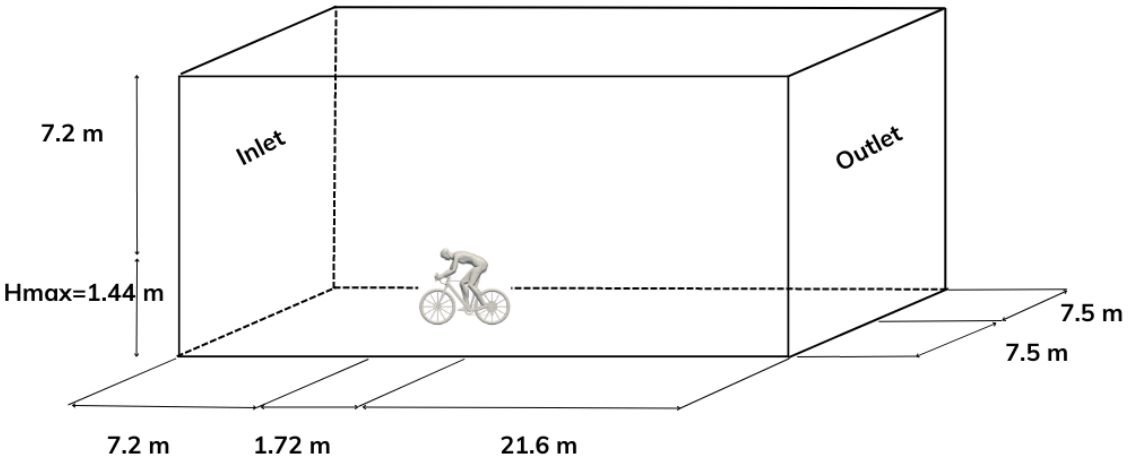

Figure 13: Computational domain with main dimensions.

The hexahedral discretized control volume generated by BlockMesh was further refined using the mesh utility SnappyHexMesh. This allowed for element refinement around the primary regions of interest. The resulting 3D mesh comprises hexahedra and splithexahedra derived from a triangulated surface geometry in Stereolithography (STL) format.
The mesh topology was defined using refinement boxes, where the original blocks are split based on the desired level of refinement. For each level value n, the cells in the base mesh are divided in each direction a number of times equal to 2^n. The refinement regions were selected based on two modes:

- Mode distance: This mode enables the definition of refinement zones with varying levels of refinement that decrease with distance from the model.
- Mode inside: In this mode, only the level value needs to be specified, and all cells inside the surface are refined up to that level.

One refinement zone was established using the mode distance approach, with a distance of 0.2 m from the surfaces

of the cyclist, frame, and wheels. Additionally, seven boxes were created with different levels of refinement, which were modified for the three meshes employed in the grid independence study.

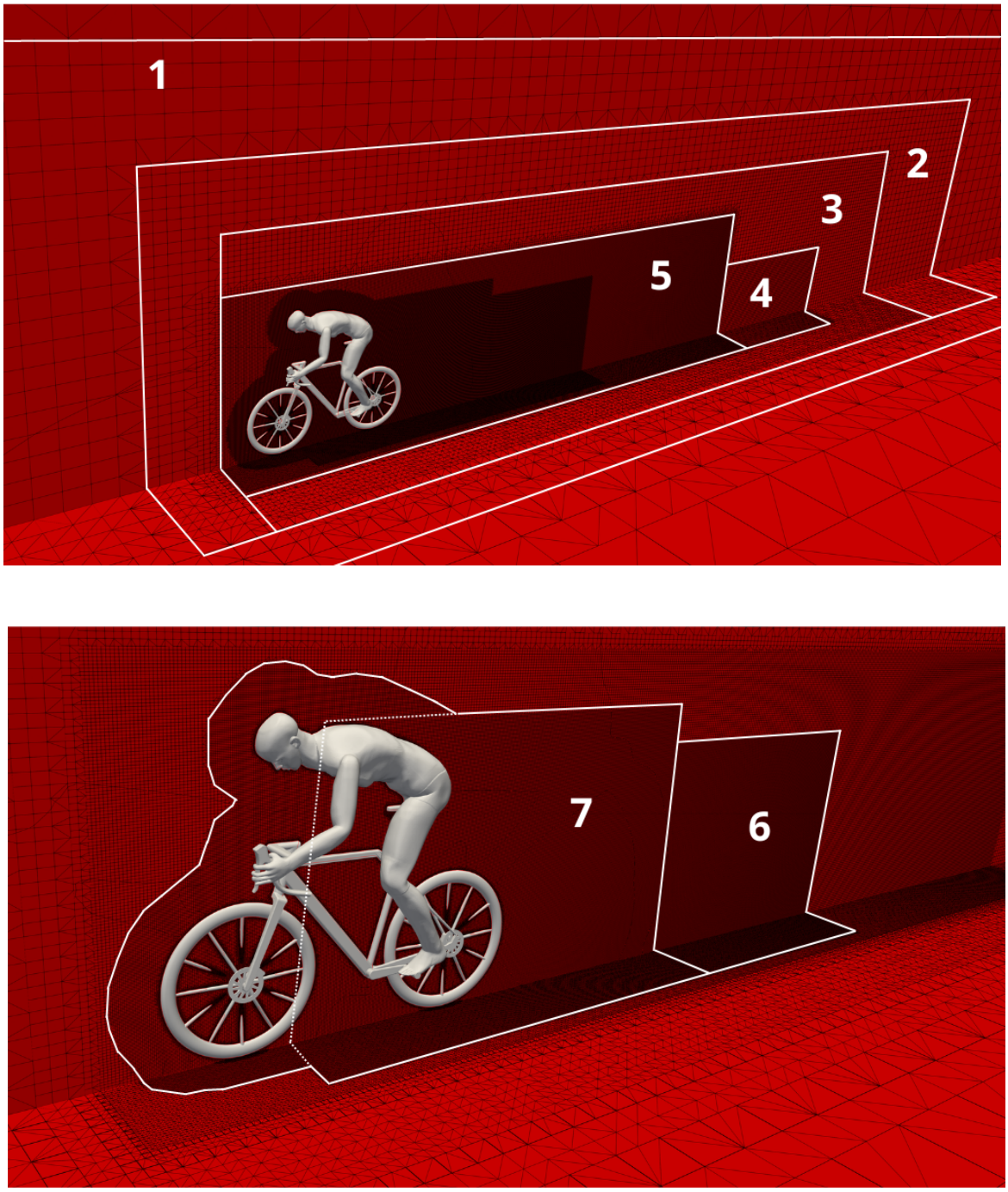

Figure 14: Computational grid with highlight of the seven boxes based on mode inside, and zoomed-in view of the refinement box based on mode distance.

One box covered the cyclist's volume, while the remaining six were designed to better capture the wake, with progressively decreasing levels of refinement. The varying levels of refinement for the different meshes are highlighted in the grid independence study.

4.1.2 Solver settings

The 3D RANS equations were solved using SimpleFoam, a steady-state solver for incompressible turbulent flow that employs the SIMPLE (Semi-Implicit Method for Pressure Linked Equations) algorithm. For turbulence modeling, the k-ω Shear Stress Transport (SST) model was adopted, which combines the Wilcox k-ω and the

k-ε models. This choice was based on the model's overall good performance in similar analyses [18], as well as its low computational cost compared to other turbulence models. A blending function activates the Wilcox model near the wall and the k-ε model in the free stream. This ensures that the appropriate model is utilized throughout the flow field. The pseudo-transient was employed for 3000 iterations with pseudo-time step of 1 s. Results were computed averaging the last 1000 iterations.

4.1.3 Boundary Conditions

At the inlet, a fixed value condition was set for the uniform velocity: 15 m/s for the grid independence study and parametric analysis, and 10 m/s for wind tunnel validation. The wheels were fixed with a rotating wall velocity dependent on the uniform velocity, following the equation $\omega = \frac{V}{R}$, where R is the wheel radius equal to 0.342 m, with the center aligned with the wheel's axis.

Flow	Inlet	Outlet	Walls	Cyclist	Wheels
k	fixedValue	inletOutlet	kqRWallFunction	kqRWallFunction	kqRWallFunction
ν	calculated	calculated	nutkWallFunction	nutkWallFunction	nutkWallFunction
Ω	fixedValue	inletOutlet	omegaWallFunction	omegaWallFunction	omegaWallFunction
p	zeroGradient	fixedValue	zeroGradient	zeroGradient	zeroGradient
U	fixedValue	inletOutlet	fixedValue	fixedValue	rotatingWallVelocity

Table 2: Boundary condition types for the CFD model specified for all variables.

For the cyclist and the bike frame a fixed value of 0 m/s was imposed, same as the bottom of the domain. At the outlet, a zero static gauge-pressure condition was set. The boundary conditions for the whole variables are shown in Table 2. FixedValue specifies the value of the variable, zeroGradient set the normal gradient of the variable to zero. The inletOutlet boundary condition is the same as zeroGradient, but it switches to fixedValue if the velocity vector next to the boundary aims inside the domain (backward flow). The value of that fixedValue is inletValue. The nutkWallFunction boundary condition provides a wall constraint on the turbulent viscosity, i.e. ν, set equal to 0. The omegaWallFunction boundary condition provides a wall constraint on the specific dissipation rate, i.e. Ω, set equal to 1.24. The kqRWallFunction boundary condition provides a simple wrapper around the zero-gradient condition, which can is used for the turbulent kinetic energy, i.e. k, set equal to 0.24. omegaWallFunction boundary condition provides a rotational velocity condition specifying axis and center of rotation.

4.1.4 Grid independence

Once the topology was set a grid independence study had to be performed. Roache [31] suggested a Grid Convergence Index (GCI) to provide a consistent manner in reporting the results of grid convergence studies and perhaps provide an error band on the grid convergence of the solution. Three levels are recommended in order to accurately estimate the order of convergence and to check that the solutions are within the asymptotic range of convergence.
The GCI is a measure of the percentage the computed value is away from the value of the asymptotic numerical value. It indicates an error band on how far the solution is from the asymptotic value and also how much the solution would change with a further refinement of the grid. A small value of GCI indicates that the computation is within the asymptotic range.
The GCI can be defined once computed some parameters. r is the refinement ratio between the three grids:

$$r = \frac{N°cells_{fine}}{N°cells_{medium}} = \frac{N°cells_{medium}}{N°cells_{coarse}}$$

and ε is the difference between two subsequent discrete solutions:

$$\varepsilon_{i+1,i} = f_{i+1} - f_i$$

In this notation, the index i indicates the grid spacing: higher index value refers to coarser grids. Once the parameter f is selected, the order of convergence p is computed:

$$p = \frac{ln(\frac{\varepsilon_{32}}{\varepsilon_{21}})}{ln(r)}$$

The theoretical order of convergence is $p = 2.0$. The difference is most likely due to grid stretching, grid quality, non-linearities in the solution, presence of shocks, turbulence modeling, and perhaps other factors. Finally, it is defined the GCI relative to the meshes:

$$GCI_{i+1,i} = \frac{F_s \, |\varepsilon|}{f_i(r^p - 1)}$$

where F_s is a factor of safety. The parameter of interest in this prior study was the drag area ($C_D A$), defined as the product between the drag coefficient (C_D) and the frontal area (A) of the model. Drag coefficient relates the drag force (F_D) to the dynamic pressure ($\rho U_\infty^2/2$):

$$C_D A = \frac{D}{\rho U_\infty^2/2}$$

Three different meshes were set to perform the independence study. The first one generated was the "Fine", with 70'550'710 cells. Therefore, gradually decreasing the refinement level in the different boxes, as shown in Table 3, the coarser grid were generated. The "Medium" resulted in 22'314'834 cells, while the "Coarse" in 7'017'083 cells. With this method, a refinement ratio r close to 3 was obtained.

Refinement Level	Box1	Box2	Box3	Box4	Box5	Box6	Box7	Distance	Surface
Coarse	2	3	4	5	5	6	6	7	8
Medium	2	3	4	5	6	7	7	7	9
Fine	3	4	5	6	6	7	8	8	9

Table 3: Refinement levels of the boxes for the three meshes used in the grid independence analysis.

The number of iterations requested to reach a convergence value was established after seeing the trend of the drag, lift and momentum coefficients. After an initial phase the trends tends to flatten. Nevertheless, as shown in Fig. 15, there were oscillations, mostly due to the coefficients relative to the body, while the ones of the bike were far more stable. For this reason, the ultimate coefficient were computed averaging the last 1000 values of the simulation.

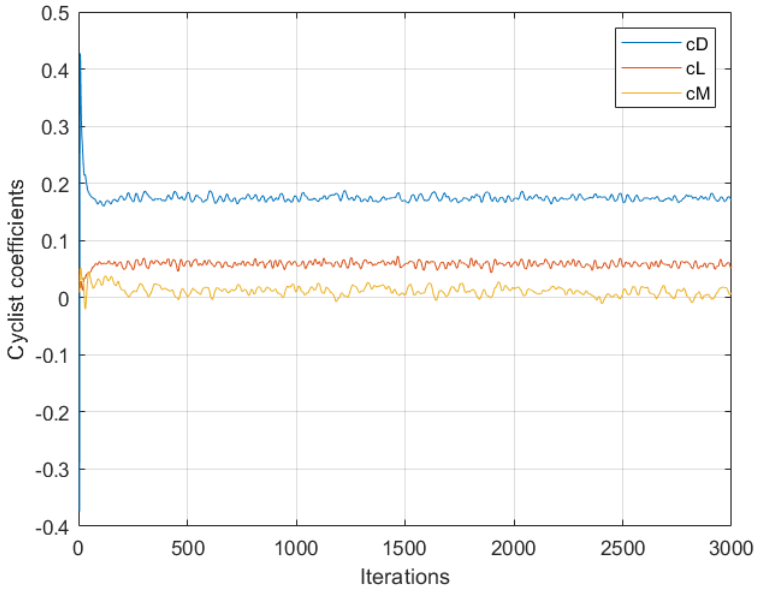

Figure 15: Variation of coefficient values with the number of iterations for the medium grid used in the grid independence analysis.

As three different grids are used in this study, the safety factor was 1.25 [28]. Otherwise, for the refinement with two grids, the safety factor is 3.0. Table 4 shows that GCI for parameter $C_D A$ from three different meshes is good with the decrement value from to ($GCI_{32} < GCI_{21}$).

	f_1	f_2	f_3	**r**	**p**	$GCI_{32}[\%]$	$GCI_{21}[\%]$
$\mathbf{C_DA}$	0.175	0.174	0.184	3	2.12	0.79	0.07

Table 4: Grid Convergence Index (GCI) data

With the two values of the GCI, it was checked that grids were in the asymptotic range of convergence

$$\frac{GCI_{32}}{GCI_{21}r^p} = 1.01 \approx 1$$

The results demonstrate that the dependency of numerical method on the mesh size has decreased, as indicated by the lower Grid Convergence Index for the finer grid compared to the coarser grid. Consequently, further refinement of the grid will not significantly affect the simulation results. Fig. 16 illustrates the error trend of the drag area for the finer grid and the coarser grid, as well as the drag area values for all three meshes. The C_DA approaches a value of approximately 0.175 m^2, with the Medium grid differing only by 0.57%. Given this small error, the Medium grid was chosen for subsequent analysis, due to its similarity in value to the Fine grid and its significantly lower computational cost. The time elapsed for the computation of the C_DA was in the order of 26 hours, for the Fine, 16 hours for the Medium and 10 hours for the Coarse.

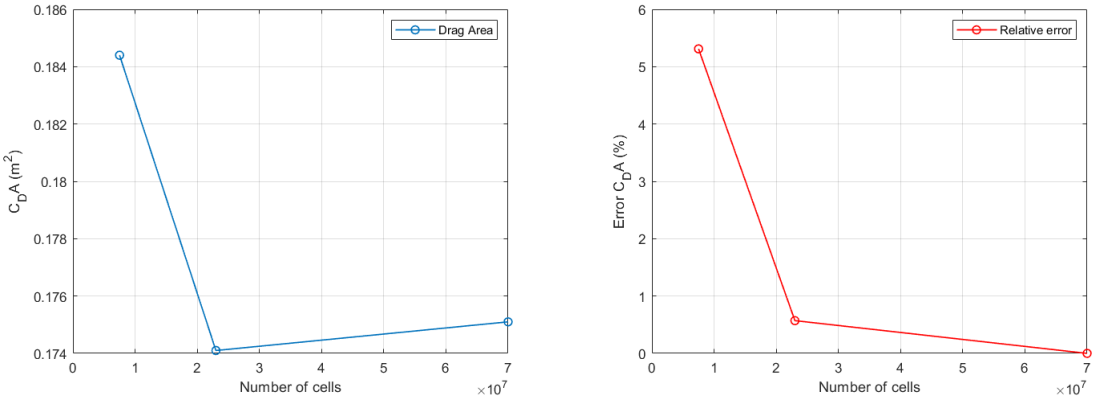

Figure 16: Comparison of drag area for three meshes used in the grid independence analysis versus the number of cells and graph of the error with respect to the finest mesh as a function of the number of cells.

4.2. Position analysis

The rigging of the virtual model opened up a wide range of possibilities. The advantage of this approach lies in the fact that the position of the mannequin can be changed to any desired position without the need to re-scan the original mannequin. This is made possible by the creation of the body's skeleton, as described in Section 2. By using inverse kinematics to move the five end-effectors and using forward kinematics to rotate and refine the position of the fingers, it becomes possible to obtain a series of different configurations for the cyclist. This section follows in the footsteps of Bert Blocken's analysis of different hill descent positions for cyclist [6], where 15 configurations were ranked in terms of aerodynamic performance. However, this research takes a different approach by using a workflow that significantly reduces the time required for this step. The advantages of this approach are numerous: the virtual model created through scanning and rigging is a faithful replica of the real athlete, allowing for natural movement with the help of the skeleton created through rigging. Recreating each of these configuration takes less than ten minutes each, and an athlete who wants to analyze the aerodynamics of a position change does not need to be physically present for additional scans or wind tunnel tests. Instead, they can obtain results from their virtual model. Therefore, the primary goal of this section is not to determine the optimal aerodynamic descent position for a cyclist, but to showcase the convenience and ease of working with a virtual model created through scanning and rigging. Five positions were selected, as shown in the figures, and were compared to the original position used for CFD simulation and printed for wind tunnel measurements. The setups were generated by utilizing the same skeleton in Blender that was used for the original configurations.

(a) Position "Original"

$A_{frontal} = 0.442\ m^2$

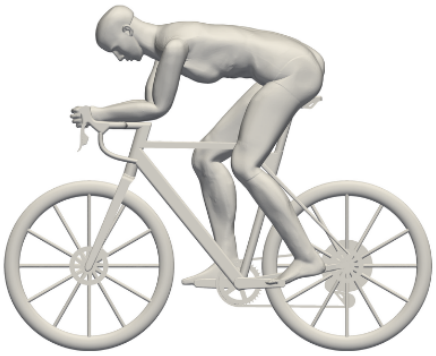

(b) Position "Elbows"

$A_{frontal} = 0.375\ m^2$

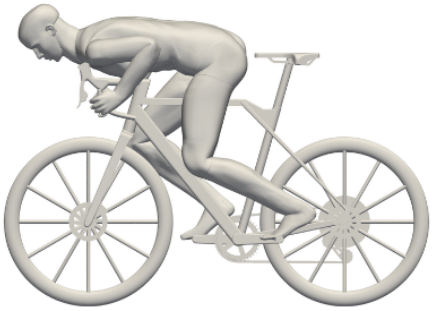

(c) Position "Froome"

$A_{frontal} = 0.357\ m^2$

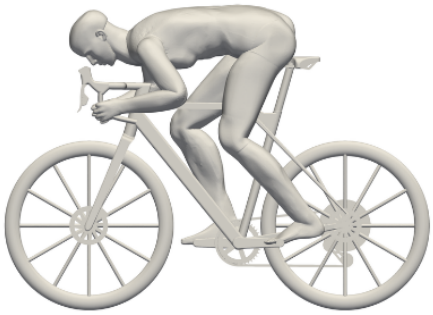

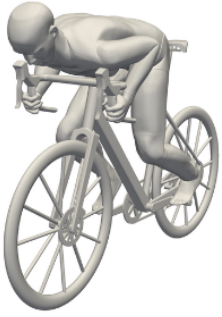

(d) Position "Aero"

$A_{frontal} = 0.368\ m^2$

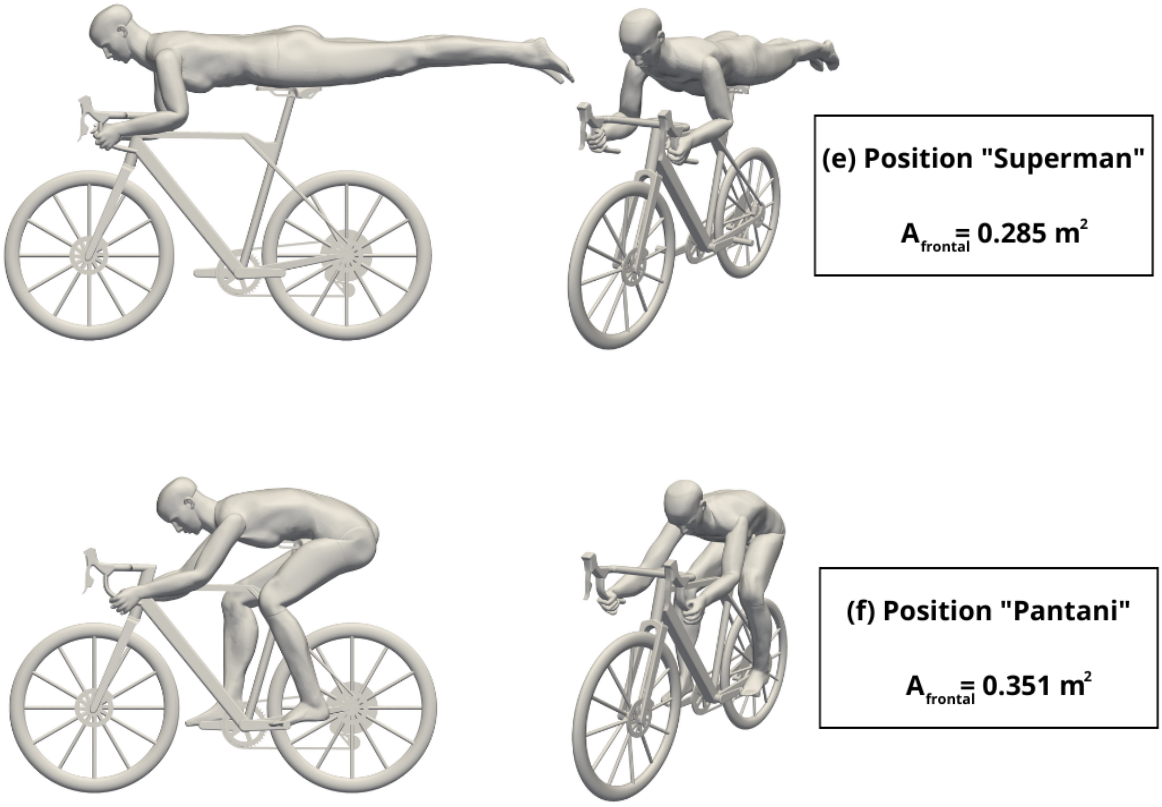

Figure 17: Side views and perspective views of the six positions. Frontal area is also indicated.

All the visualization were obtained through the Paraview 5.11.0 software.
(a) is renamed "Original" position since it was the first one obtained through rigging animation and subsequently 3D printed. It was also used for grid independence analysis. (b) The "Elbows" position is exactly the same as the initial configuration, except for the position of the arms. In this position, the cyclist does not hold the handlebar with the hands but lean on top of it through the elbows; (c) is the "Froome" position, named after the famous british athlete, refers to a position where, during stage 8 of the 2016 Tour de France, he caught the attention of viewers by pedalling with his bum on the top tube and his chest pressed against the top of the bars; (d) is another aerodynamic configuration, referred to as the "Aero" position, which involves holding the hands below the handlebar, while the back is nearly aligned with the direction of the flow. (e) "Superman", although not allowed in racing competitions, is chosen for its iconic nature and provides valuable insights in aerodynamic analysis. In this position, the athlete presses their belly on the saddle, while the legs and back are perfectly aligned with the flow. Last is the (f) "Pantani" position, named after its creator, who achieved a speed of 78 km/h during a famous descent using this configuration. The time required to recreate each of these positions using Blender is within ten minutes. This highlights the potential of rigging animation implemented to recreate cyclist positions. In a realistic scenario, where an athlete wants to test one or more new configurations, they can rely on their virtual model, which can be moved to the desired position, saving a considerable amount of time compared to not having these tools available.
After exporting the simulations in STL format, CFD analysis were performed. The virtual cyclist was once again in a full-sized, static position. The computational domain, solver settings and the boundary conditions remained identical to those presented in the Section 4.1. Wind velocity was set to 15 m/s, to recreate a realistic racing condition and the simulations were again run for 3000 iterations, with the results computed averaging the last 1000 steps.
The C_DA of the six configurations are shown in the figure below. The position which yielded the lower drag area was the "Superman" position, with a value of 0.129 m^2, primarily due to its small frontal area. The second best-position was the "Pantani" with a drag area of 0.138 m^2. The remaining four configurations showed significant differences from each other and from the top two. The "Elbows" position had a drag area of 0.161 m^2, followed by the "Froome" with 0.165 m^2 and the "Aero" with 0.168 m^2. The worst was, as expected, the "Original" configuration, 0.174 m^2, as it was not aerodynamically optimized.

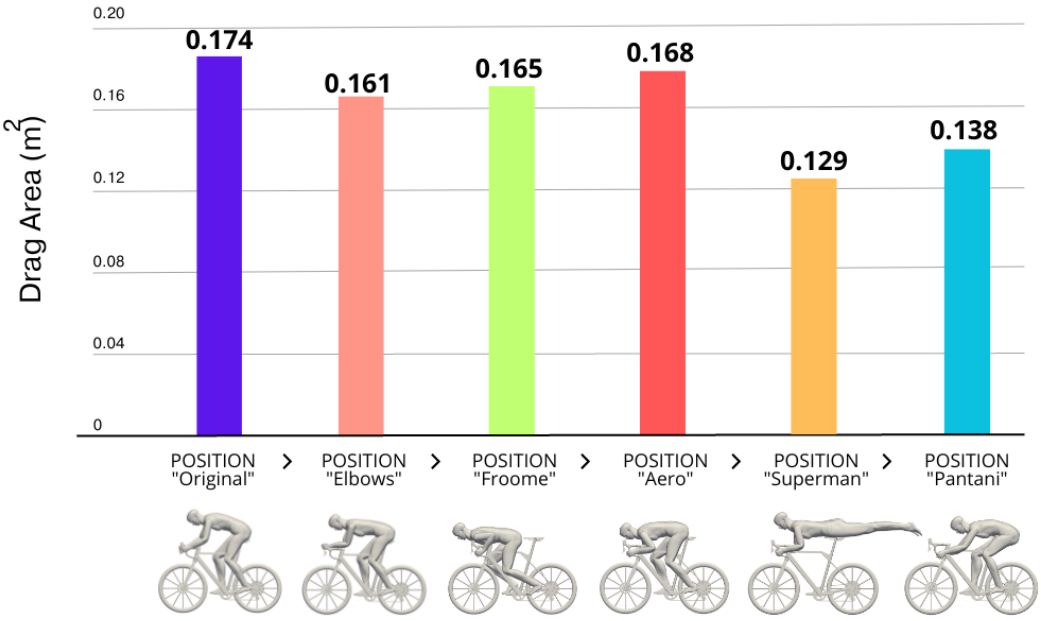

Figure 18: Comparison of CFD results for the six positions in terms of drag area.

Further insights into this aerodynamic trend were obtained by plotting the velocity streamlines around the six cyclists. Each figure represents the visualization of the pressure on the body surface, while the streamlines are color-coded based on the velocity magnitude. The lines were generated starting from the same position for all configurations to ensure a proper comparison, passing along the bike's axis of symmetry. For the "Original" position, it is clear that the flow is significantly perturbed by the mannequin's position, which also has the largest frontal area among the six. This results in the highest aerodynamic drag. The poor performance of this position is further exacerbated by the inclination of the back relative to the flow direction, which is the only one not aligned with it. For the "Aero" position, there are noticeable lower pressure zones, represented by darker colors. These zones are observed behind the right arm and on the back, particularly in the rib area. These factors contribute to increased aerodynamic drag, as they create a suction effect that pulls the cyclist backward. However, compared to the "Original" configuration, there are still clear improvements, as the upper body is more streamlined. The favorable performance of the "Elbows" position is due, in part, to the position of the arms, which are not extended to the ends of the handlebar but rather lie centrally. Hence, the upper body is "shielded" and its contribution to the resistance force is reduced. Although the flow is still perturbed by the presence of the arms, less of the torso and legs are exposed to the wind due to the shielding effect.

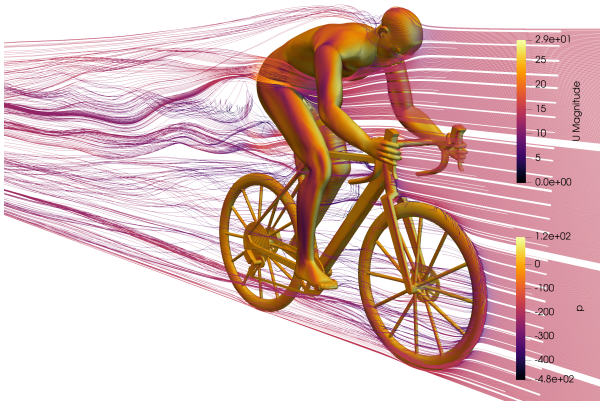

(a) "Original" position

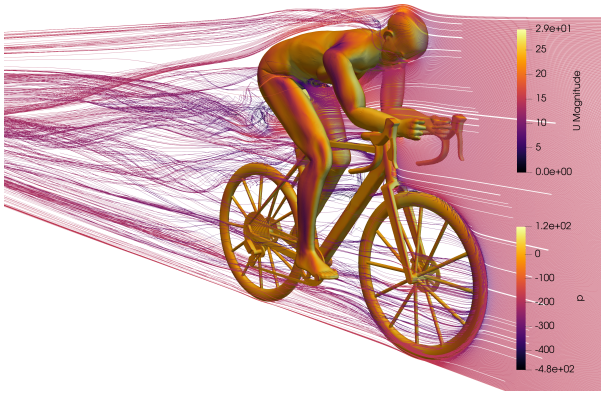

(b) "Elbows" position

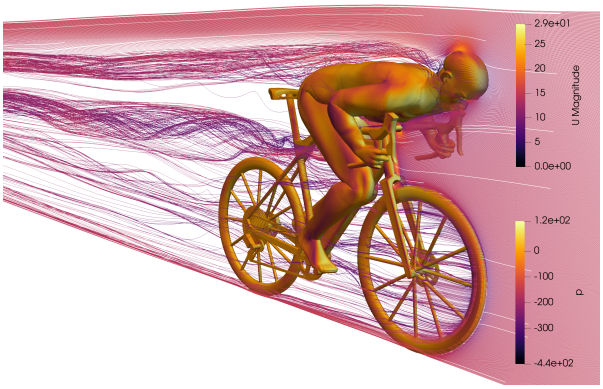

(c) "Froome" position

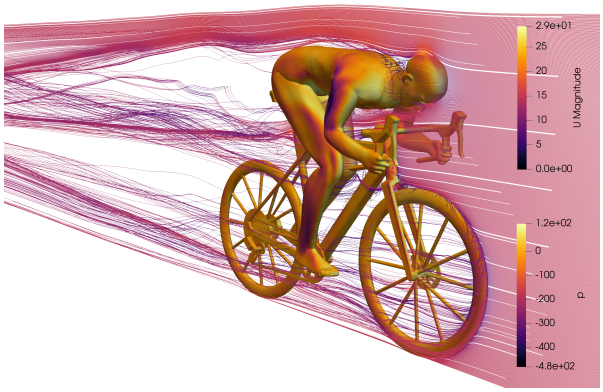

(d) "Aero" position

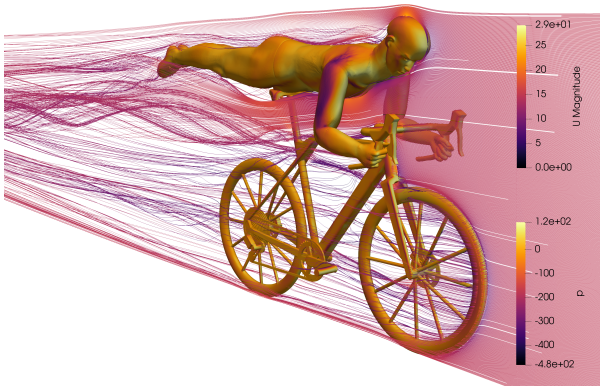

(e) "Superman" position

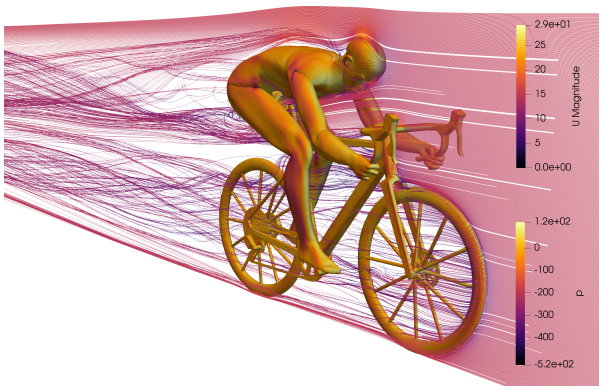

(f) "Pantani" position

Figure 19: Perspective view of the visualization of vertical velocity streamlines passing along the bike axis for the six positions, and pressure distribution on the bike and cyclist surfaces. The visualization is complemented with a scale indicating the magnitude of velocity and pressure.

For the "Superman" position the presence of low pressure zones along the side of the left arm is evident. However, these zones do not contribute to drag, as the generated force is directed perpendicularly to the flow velocity. The smallest frontal area compared to the other five configurations is one of the main reason for the lower drag area, as the form drag component is significantly decreased. In this position, the legs have minimal effect on the resistance force, since they are aligned with the free-stream, and the flow passing through those zones is already perturbed by the torso.
Further analysis can be conducted by examining the isosurfaces for the total pressure coefficient, which is defined as:

$$C_{p_{tot}} = \frac{p + 1/2\rho U^2}{1/2\rho U_\infty^2} \quad \text{for } \rho = 1$$

where p is the static pressure and U the velocity magnitude computed locally in the volume. Isosurfaces represent parts of the volume mesh where a specific parameter assumes a certain value. In this case, the parameter is the total pressure coefficient, which represents the ratio between the total pressure and the free-stream dynamic pressure, set to zero.
This visualization technique helps identify the areas contributing to drag, as anything inside these volumes corresponds to low-pressure regions that slow down the cyclist. The analysis of the isosurfaces is supported by visualizing the distribution of the total pressure coefficient over the body and bike surfaces. The coefficient range has been normalized from -1 to 1 for a better visibility, divided into 12 coloured subranges. Similar characteristics can be observed across the six configurations. Looking at the values of the toal pressure coefficient, low pressure zones are evident on the sides of the arms, and on the upper part of the body, except for the "Froome" position, where they are located on the forearms. Additionally, the sides of the legs and the back of the head show low values of the pressure coefficient, except for the "Superman" position, where the alignment of the legs with the wind speed prevents this pressure decrease.
It should be noted that these low pressure zones do not contribute significantly to drag, as the force generated by

this distribution is perpendicular to the flow direction. On the other hand, higher pressure zones are dominant on the surfaces that face the flow perpendicularly, such as the front head where the stagnation point is located. This is why drag increases with a larger frontal area. Even analyzing the isosurfaces, it is evident that there are common areas between the six positions: these zones obviously are the bike's parts, such as the front wheel and the bike frame, which contribute identically to drag, while the isosurfaces generated on the rear wheel are dependent of the cyclist configuration.

(a) "Original" position

(b) "Elbows" position

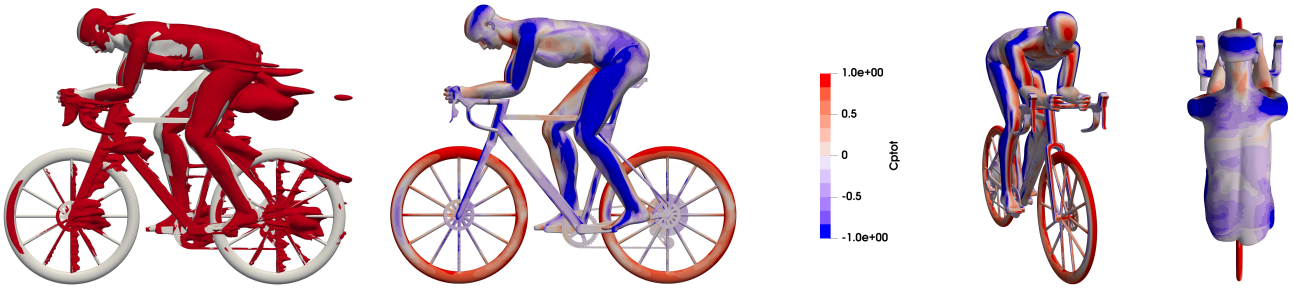

(c) "Froome" position

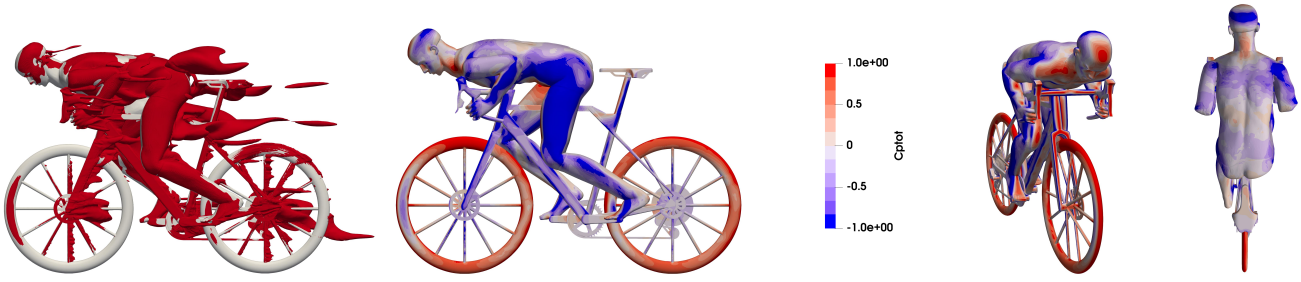

(d) "Aero" position

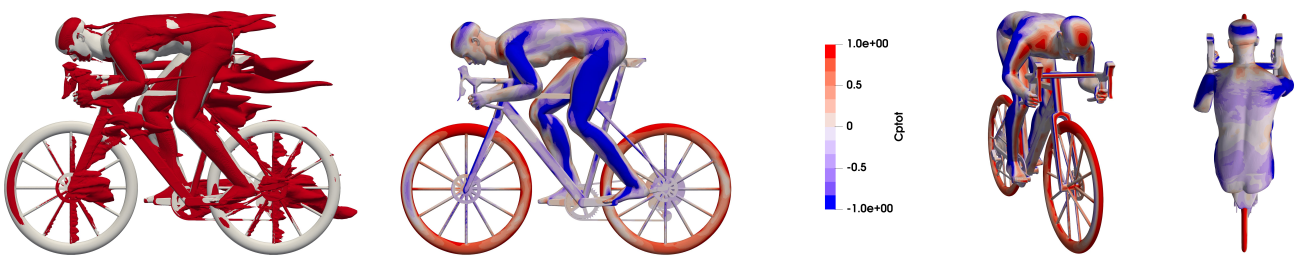

(e) "Superman" position

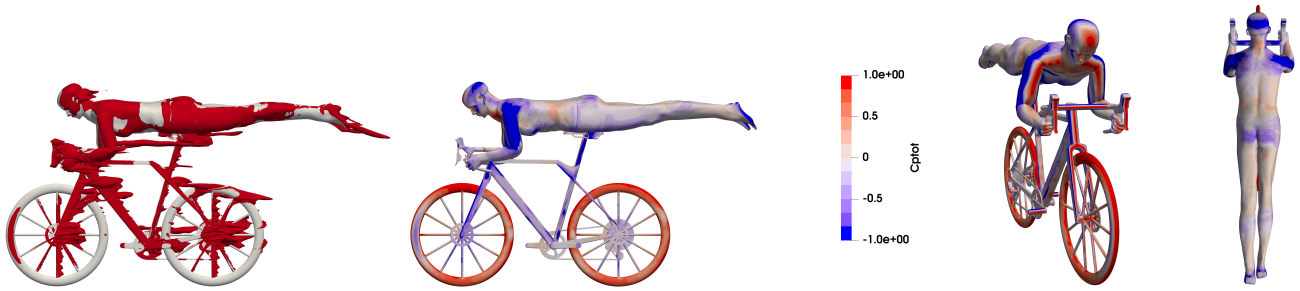

(f) "Pantani" position

Figure 20: Total pressure coefficient on cyclist and bicycle surfaces, and isosurfaces for $C_{p_{tot}}$ =0

The most evident separation zones occur along the leg and the arm sides, and in correspondence of the neck, where the flow then reattach on the back. Still, each configurations has its behaviour. The "Original" position is the one which generates the biggest bubbles behind the body, which contribute significantly to drag. This configuration is also associated with the highest frontal area, hence it has the most high-pressure body surfaces. For the "Superman" configuration there are only few zones of separation. Since the body is horizontally aligned, the lower back does not contribute to generating significant bubbles, and the flow remains attached to the body surface until the foot. This is a crucial difference compared to the other five positions, where the legs are bent to stay on pedals and face the flow, thereby increasing overall drag. Additionally, the configuration's minimal frontal area plays a significant role in reducing form drag. The "Pantani" position is characterized by the longest bubble generated at the back, indicating a strong pull-back effect in this zone. however, there are not many other body surfaces leading to separation. Notably, the position of the legs in this configurations appears to avoid generating any low-pressure zones. The effectiveness is likely attributed to the positioning of the arms. Apart from the "Superman" position, the elbows do not form a high angle between the lower and upper arm, resulting in a more streamlined configurations for the cyclist and minimizing separation bubbles.

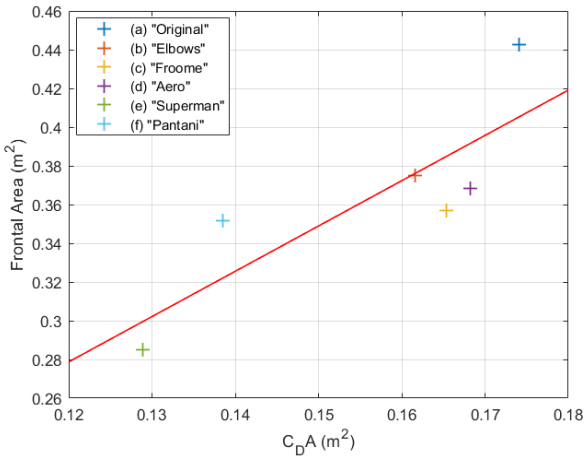

Figure 21: Drag area versus frontal area for all six positions, and mean trend line.

Fig. 21 illustrates the trend of the six drag areas compared to their correspondent frontal areas. As mentioned earlier, the configurations with the smallest and the largest frontal area, namely the "Superman" and "Original" positions, respectively, exhibit the lowest and highest drag area, However, this correlation does not always hold true. In fact, among these six positions, there is no monotonic increase in the drag area with an increase in the frontal area. "Elbows" position, despite having a larger frontal area than the "Froome" and "Aero" positions, actually produces a lower drag area than those two. Another notable peculiarity is observed in the "Pantani" position, which has a nearly identical frontal area compared to the "Froome" and "Aero" positions, yet exhibits a significantly lower drag area. The graph also displays the line of best fit, which is a straight line that minimizes the distance between the line and data points. This line helps visualize the performance of different configurations compared to the mean trend. Configurations that lie above the line, such as the "Pantani" and "Original" position, perform better than the mean trend, as they would yield a larger drag area if their projection had the same frontal area. Conversely, configurations that lie below the line, such as "Froome", "Aero", and "Superman", perform worse than the mean trend. This indicates that the aerodynamic position of a configuration, given the same frontal area, is not optimal.

5. Conclusions

A new workflow for investigating the aerodynamics of a cyclist has been implemented. The starting point consisted of 3D scanning a life-sized mannequin in standing position. Through the rigging technique in Blender software, the model was animated, by placing a simplified skeleton inside the mannequin to mimic human movements. By utilizing inverse and forward kinematic, a cycling position was achieved by moving the five end-effectors: hands, feet and torso. The virtual model was then placed on a Canyon racing bike and prepared for 3D printing, resulting in a scaled-down physical copy. The virtual copy was used for CFD simulations, starting with a grid independence study based on the Grid Convergence Index, with the drag area as the parameter of interest. Once it was found the mesh that didn't require further refinement for increased accuracy, a comparison between six cyclist configurations was conducted. All simulations were performed with the model in a static position, without pedaling. The six positions were obtained using the same rigging model used to convert the standing mannequin into the original cyclist position, with the cyclist being moved to assume different configurations. Analysis of velocity streamlines and total pressure coefficients distribution were performed to gain insights into the aerodynamic behavior of each position.
In summary, the aim of the research was to develop a workflow that allows for aerodynamic testing using a fully virtual athlete. The virtual copy of the cyclist can be moved to recreate different racing configurations without the need for the physical presence of the person. The main motivation behind that scope was to reduce the time and money that nowadays are spent: an athlete invests a couple days to perform wind tunnel tests, possibly including the time to transfer from his current location to where wind tunnel is. Although having a 3D printed copy of the athlete can be useful it is constrained to test a singular position, and additional scans would be necessary to compare multiple configurations. The time frames of each step are reported:

- Model preparation and scanning - 15 minutes
- Data post-processing in the scanning software - 2 hours
- Rigging and cyclist animation on Blender - 1 hour
- Change of position on Blender - 10 minutes

Once these steps are covered the virtual model is ready for CFD simulations. The potential of Computational Fluid Dynamic is well-known, as it allows for various types of simulations, such as analyzing crosswind effects, yaw angles, and changes in velocity by adjusting the CFD solver settings and boundary conditions. Combining 3D scanning and rigging technique:, athletes' phsyical presence is only required during the initial scanning phase. Afterward, a physical copy can be 3D printed for wind tunnel validation or for designing ad-hoc equipment such as skinsuits or handlebar. Additionally, athletes can easily make slight changes in their positions virtually within minutes, eliminating the need for repeated wind tunnel sessions or rescanning.
The potential of these combined techniques was demonstrated following the footsteps of the famous Bert Blocken analysis of different cyclist hill positions. A fundamental difference lies in the time spent: in that study, the athlete had been scanned as many times as the number of position tested, and additional configurations could have been added only based on the athlete's availability (in the case of a professional cyclist, their schedule can be very busy, making it complex to find time for researching). In contrast, in this work, the positions are obtained within ten minutes. This highlights the potential of rigging animation implemented to recreate cyclist positions. In a realistic scenario, where an athlete wants to test one or more new configurations, they

can rely on their virtual model, which can be moved to the desired position, saving a considerable amount of time compared to not having these tools available. Despite the diversity in cyclist size, structure, bike, solver, boundary conditions as well as the challenge of recreating the same iconic positions, a similar trend to Blocken's findings is observed:

- The fastest configuration turned out to be the "Superman" position due to its small frontal area. The horizontal alignment of the legs with the torso dragged down the resistance force.
- The "Original" position used for initial tests is the slowest. The configuration was not optimized for improving aerodynamic efficiency since it only constituted a baseline for any position change.
- Second fastest position among these six is the "Pantani" one, consistent with Blocken analysis.
- The remaining three positions yield drag area values close to each other. Notably, the "Froome" position, characterized by the higher frontal area among the three, is associated to the lower drag area, meaning that an increasing in the frontal area doesn't necessarily correlate with an increase in the drag area.

An important remark must be made about the position analysis. The comparison aimed to highlight in terms of frontal and drag area how the configurations behave, from an aerodynamic point of view only. Hence, the study does not investigate the equally important side of the power generation: the most aerodynamic position for a cyclist means nothing if the athlete is not able to generate a proper amount of power. Although Blocken focuses on the hill descent position, in which the athlete is not forced to pedal, another significant trade-off must be taken into account. Besides finding the configuration that offers the lowest drag force, it is also important to consider a position that does not physically penalized the cyclist, particularly in terms of breathing.
The workflow was developed with obvious approximations, which can be resolved more accurately in the future. The main challenges involves the creation of the rig for the mannequin. The number of bones used represented only about a quarter of the overall human skeleton. Although the joints were placed in attempt to best fit the mannequin, the initial position of the model made the operation more difficult, resulting in potential errors in recreating the body movements. This was the most delicate step, as even the smallest changes in joint position could lead to an incorrect motion system. Further studies could focus on improving this aspect to achieve a model that is closer to reality. During this research, an approximation was made to have the cyclist in a static position without any pedalling effect. Future works could investigate this aspect, both by incorporating a moving mannequin and conducting unsteady simulations in Computational Fluid Dynamics (CFD). Moreover, the most interesting step would be to apply the entire workflow to a real athlete. The challenge would be to achieve an exact correspondence between the movements recreated through rigging animation and the those the cyclist can actually perform. In addition, the scan process would become more complex since a mannequin does not exhibit any natural movements. The ultimate goal of this paper is to lay the foundation for developing a method that can be useful for both elite and amateur athletes. While simplifications have been made, the workflow remains the core of this and future projects.

References

[1] Mark Adams, Erick Miller, and Max Sims. *Inside Maya 5.* 2003.

[2] Artec Europe. Artec leo, 3d scanners, 2018.

[3] Ilya Baran and Jovan Popović. Automatic rigging and animation of 3d characters. *ACM Trans. Graph.*, 26(3):72–es, jul 2007.

[4] Marco Belloli, Stefano Giappino, Fabio Robustelli, and Claudio Somaschini. Drafting effect in cycling: Investigation by wind tunnel tests. *Procedia Engineering*, 147:38–43, 2016. The Engineering of SPORT 11.

[5] Bert Blocken and Yasin Toparlar. A following car influences cyclist drag: Cfd simulations and wind tunnel measurements. *Journal of Wind Engineering and Industrial Aerodynamics*, 145:178–186, 2015.

[6] Bert Blocken, Thijs van Druenen, Yasin Toparlar, and Thomas Andrianne. Aerodynamic analysis of different cyclist hill descent positions. *Journal of Wind Engineering and Industrial Aerodynamics*, 181:27–45, 2018.

[7] Bert Blocken, Thijs van Druenen, Yasin Toparlar, Fabio Malizia, Paul Mannion, Thomas Andrianne, Thierry Marchal, Geert-Jan Maas, and Jan Diepens. Aerodynamic drag in cycling pelotons: New insights

by cfd simulation and wind tunnel testing. *Journal of Wind Engineering and Industrial Aerodynamics*, 179:319–337, 2018.

[8] Toparlar Y. et al. Blocken B., van Druenen T. Cfd analysis of an exceptional cyclist sprint position. *Sports Eng 22 10*, 2019.

[9] Anthony Bouillod, Luca Oggiano, Georges Soto-Romero, Brunet Emmanuel, and Fred Grappe. Preliminary study: A new method to assess the effective frontal area of cyclists. 11 2016.

[10] João Brito, Luís Lopes, Ana Conceição, Aldo Costa, and Hugo Louro. Maximal cycling tests under velodrome and laboratory conditions. *Journal of Human Sport and Exercise*, (in press), 01 2014.

[11] Len W. Brownlie. *Wind Tunnels: Design Considerations in Wind Tunnel Testing of Cyclists*, pages 57–86. Springer International Publishing, Cham, 2019.

[12] RB Candau, F Grappe, M Ménard, B Barbier, GY Millet, MD Hoffman, AR Belli, and JD Rouillon. Simplified deceleration method for assessment of resistive forces in cycling. *Medicine and science in sports and exercise*, 31(10):1441—1447, October 1999.

[13] S. Chi, Pitman J., Crouch T., Burton D., and Thompson M. The application of body scanning, numerical simulations and wind tunnel testing for the aerodynamic development of cyclists. *Proceedings of the Institution of Mechanical Engineers, Part P: Journal of Sports Engineering and Technology.*, 235(4):339–353, 2021.

[14] Harun Chowdhury, Firoz Alam, and David Mainwaring. A full scale bicycle aerodynamics testing methodology. *Procedia Engineering*, 13:94–99, 12 2011.

[15] Timothy N. Crouch, David Burton, Mark C. Thompson, Nicholas A.T. Brown, and John Sheridan. Dynamic leg-motion and its effect on the aerodynamic performance of cyclists. *Journal of Fluids and Structures*, 65:121–137, 2016.

[16] Huan Dai, Bo Cai, Jia xing Song, and Dengyi Zhang. Skeletal animation based on bvh motion data. *2010 2nd International Conference on Information Engineering and Computer Science*, pages 1–4, 2010.

[17] Thijs Defraeye, Bert Blocken, Erwin Koninckx, Peter Hespel, and Jan Carmeliet. Aerodynamic study of different cyclist positions: Cfd analysis and full-scale wind-tunnel tests. *Journal of Biomechanics*, 43(7):1262–1268, 2010.

[18] Thijs Defraeye, Bert Blocken, Erwin Koninckx, Peter Hespel, and Jan Carmeliet. Computational fluid dynamics analysis of cyclist aerodynamics: Performance of different turbulence-modelling and boundary-layer modelling approaches. *Journal of Biomechanics*, 43(12):2281–2287, 08 2010.

[19] TU Delft. A 3d printed mannequin of tom dumoulin in the tu delft wind tunnel helps gain a competitive advantage, 2016.

[20] Easton Cycling. Defining, measuring and improving aerodynamic testing in the bicycle industry, 2013. `https://www.aerosportsresearch.com/pdf/easton-aero-wp.pdf`.

[21] D.M. Fintelman, Hassan Hemida, Mark Sterling, and François-Xavier Li. Cfd simulations of the flow around a cyclist subjected to crosswinds. *Journal of Wind Engineering and Industrial Aerodynamics*, 144:31–41, 09 2015.

[22] Jörg Franke and Alexander Baklanov. *Best Practice Guideline for the CFD Simulation of Flows in the Urban Environment: COST Action 732 Quality Assurance and Improvement of Microscale Meteorological Models*. 01 2007.

[23] Juan Garcia-Lopez, Ana Ogueta-Alday, Josu Larrazabal, and Jose Rodriguez-Marroyo. The use of velodrome tests to evaluate aerodynamic drag in professional cyclists. *International journal of sports medicine*, 35:451–455, 05 2014.

[24] Frederic Grappe, Robin Candau, Alain Belli, and Jean Denis Rouillon. Aerodynamic drag in field cycling with special reference to the obree's position. *Ergonomics*, 40(12):1299–1311, 1997.

[25] Mohd Javaid, Abid Haleem, Ravi Pratap Singh, and Rajiv Suman. Industrial perspectives of 3d scanning: Features, roles and it's analytical applications. *Sensors International*, 2021.

[26] Houigab Jeong, Seungho Lee, and Soon-Duck Kwon. Blockage corrections for wind tunnel tests conducted on a darrieus wind turbine. *Journal of Wind Engineering and Industrial Aerodynamics*, 179:229–239, 08 2018.

[27] M. Kordi, Galis G., Erp TV., and Terra W. Reliability and sensitivity of the notio konect to quantify coefficient of drag area in elite track cyclists. *European Journal of Sport Science.*, 22(6):774–779, 2022.

[28] B. E. Launder. Turbulence modelling for cfd. by d. c. wilcox. dcw industries inc., 1993. 460pp. *Journal of Fluid Mechanics*, 289:406–407, 1995.

[29] Paul Mannion, Yasin Toparlar, Bert Blocken, Magdalena Hajdukiewicz, Thomas Andrianne, and Eoghan Clifford. Improving cfd prediction of drag on paralympic tandem athletes: influence of grid resolution and turbulence model. *Sports Engineering*, 21(2):123–135, 10 2018.

[30] L. Mikahila. Italian national cycling team improves aerodynamics using calibry 3d scanner, 2021.

[31] P.J. Roache. Perspective: A method for uniform reporting of grid refinement studies. *Journal of Fluids Engineering*, 116(3):405–413, 09 1994.

[32] Team Jumbo Visma. Roglic has his own 3d model at tu eindhoven, 2020.

[33] Vorteq. Artec leo helps vorteq create the world's fastest cycling skinsuits, 2021.

Abstract in lingua italiana

La riduzione della resistenza aerodinamica è un aspetto cruciale nel ciclismo. Attualmente, per ottimizzare l'aerodinamica, gli atleti si affidano a test in galleria del vento, simulazioni CFD o esperimenti in velodromo, che comunque richiedono la validazione tramite misurazioni in galleria del vento. Ogni nuovo test richiede quindi significativi investimenti in termini di risorse finanziarie e di tempo, aspetto vitale nella vita professionale di un ciclista. Questa ricerca introduce un nuovo metodo di lavoro che mira a semplificare ed accelerare il processo di analisi aerodinamica nel ciclismo. Il flusso di lavoro è focalizzato sull'utilizzo di un manichino a grandezza naturale ed integra simulazioni CFD, validazione in galleria del vento, scansione 3D e tecniche di animazione "rigging", realizzate con Blender. Tali tecniche prevedono la creazione di uno scheletro virtuale che consente di posizionare il modello scansionato in qualsiasi posizione desiderata, eliminando la necessità di cambiamenti e test fisici. Per dimostrare i vantaggi in termini di risparmio di tempo di questo approccio, sei diverse configurazioni ottenute utilizzando il modello con animazione sono confrontate con analisi CFD in termini di resistenza aerodinamica, linee di velocità e distribuzione dei coefficienti di pressione. L'intero processo dalla scansione iniziale del manichino al raggiungimento della posizione desiderata impiega approssimativamente tre ore, riducendo significativamente il tempo richiesto rispetto ai metodi tradizionali. Inoltre, è possibile apportare facilmente modifiche future alla posizione o all'equipaggiamento utilizzando il modello virtuale. Integrando tecniche virtuali con simulazioni CFD e validazione in galleria del vento viene consentita una valutazione rapida delle prestazioni aerodinamiche in modo più efficiente ed economico.

Parole chiave: Aerodinamica nel ciclismo, Scan 3D, Fluidodinamica computazionale, Rigging, galleria del vento, Posizione ciclista

Acknowledgements

I would like to express my sincere gratitude to my thesis advisor, Professor Paolo Schito, for his guidance, expertise, and support throughout the entire research process.
I would also like to extend my appreciation to my co-advisors, Marco Rossoni and Claudio Somaschini, for their invaluable contributions to this thesis.
Furthermore, I would like to express my gratitude to my entire family, which has supported me from the day of my admission until the last day of my studies, and for their understanding and motivation during this period.
I would also like to remember and acknowledge all the people who have been put in my journey. My girlfriend, my colleagues, my friends, those I have known for a long time, those I have met during these years, and those who have taken a different path in life. Anyone who has shown interest in my work and offered even a simple word has provided a priceless motivation for me.
Thank you all for being an integral part of this journey.